Synthesis and characterization of proton-conducting Ba(Zr0.8-xCexY0.2)O2.9 ceramics

Authors: R. R. Chien, S.-S. Tu, V. Hugo Schmidt, S.-C. Lee, and C.-C. Huang

R.R. Chien, S.-S. Tu, V.H. Schmidt, S.-C. Lee, and C.-C. Huang, "Synthesis and characterization of proton-conducting Ba(Zr0.8-xCexY0.2)O2.9 ceramics," Solid State Ionics 181, 1251-1257 (2010). doi: 10.1016/j.ssi.2010.07.024.

Synthesis and characterization of proton-conducting $Ba(Zr_{0.8-x}Ce_xY_{0.2})O_{2.9}$ ceramics

R.R. Chien [a,*], C.-S. Tu [b,c], V. Hugo Schmidt [a], S.-C. Lee [c], C.-C. Huang [c]

[a] Department of Physics, Montana State University, Bozeman, MT 59717, USA
[b] Graduate Institute of Applied Science and Engineering, Fu Jen Catholic University, Taipei, Taiwan 242, ROC
[c] Department of Physics, Fu Jen Catholic University, Taipei, Taiwan 242, ROC

A B S T R A C T

X-ray diffraction and micro-Raman scattering have been used to characterize the effects of glycine-to-nitrate (G/N) and zirconium-to-cerium (Zr/Ce) molar ratios on structural properties of proton-conducting $Ba(Zr_{0.8-x}Ce_xY_{0.2})O_{2.9}$ (BZCY) ceramic powders fabricated by using the glycine–nitrate combustion method. Particle sizes of as-synthesized and calcined BZCY powders are estimated by using the Scherrer's formula, and are sensitive to G/N and Zr/Ce ratios. A simple cubic perovskite phase is observed for calcined $Ba(Zr_{0.7}Ce_{0.1}Y_{0.2})O_{2.9}$ powders fabricated with G/N ratios of 1/3–3/4. Calcined BZCY ($x = 0.0$–0.8) powders fabricated with $G/N = 1/2$ exhibit a single-phase structure and a structural transformation from cubic to possibly rhombohedral for $Zr/Ce \leq 2/6$. Particle sizes of as-synthesized and calcined BZCY ($x = 0.0$–0.8) powders fabricated with $G/N = 1/2$ vary in the ranges of 5–15 and 34–42 nm, respectively. In-situ temperature-dependent linear shrinkage measurement reveals that smaller-particle BZCY powder can reach densification at a considerable lower temperature.

1. Introduction

Perovskite-type $(Ba,Sr,Ca)(Zr,Ce)O_3$ oxides exhibit good protonic conduction under hydrogen-containing atmosphere at elevated temperature. In pioneering work on these materials, Iwahara noted that they are promising for applications of proton-conducting solid oxide fuel cells (H-SOFCs), hydrogen separation membranes, hydrogen pumps, hydrogen sensors, and steam electrolyzers for hydrogen production [1–3]. Some of that promise was recently fulfilled, in a 2005 report by Taniguchi et al. [4] on a hydrogen sensor based on $BaZr_{0.4}Ce_{0.4}In_{0.2}O_3$. The early SOFC experiments by Iwahara were on electrolyte-supported cells, so it was not possible to obtain high power densities.

In recent work, hydrogen-fueled anode-supported H-SOFCs with BZCY electrolytes made by Yang et al. [5] achieved power density of 700 mW/cm^2 at the relatively low temperature of 700 °C and 860 mW/cm^2 at 750 °C, and BZCY-based cells made by Meng et al. [6] reached 371 mW/cm^2. In 2009, Yang et al. [7] attained 1100 mW/cm^2 at 750 °C with a cell having $BaZr_{0.1}Ce_{0.7}Y_{0.2-x}Yb_xO_{3-\delta}$ electrolyte in which the Yb is claimed to enhance O^{2-} vacancy conduction to complement the protonic conduction. Our group is obtaining comparable power densities with BZCY- and BCY-based cells [8]. For instance, a BCY cell with 60% H_2 and 40% N_2 fuel mix achieved 900 mW/cm^2 power density at 750 °C.

These power densities are competitive with those achieved by O-SOFCs with oxygen ion conducting electrolytes. H-SOFCs have two advantages over O-SOFCs, based on the fact that on the anode side there is only hydrogen inflow, with no steam outflow. First, higher fuel utilization can be achieved because there is no loss of fuel flowing out with the steam exhaust gas. Second, anode-supported cells having a relatively thick anode are desirable because the anode has a strong metal (usually Ni) framework, and there is much less fuel pressure loss through the anode passages in H-SOFCs because there is no steam counterflow.

Cerate-based proton conductors have a high ionic conductivity but exhibit poor chemical stability in CO_2, H_2O, and H_2S containing atmosphere at elevated temperature [9–11]. Although zirconate-based proton conductors have lower ionic conductivity, they show good chemical and mechanical stabilities [12]. By thermal analysis and x-ray diffraction (XRD), $Ba(Ce_{0.9}Y_{0.1})O_{3-\delta}$ powder was confirmed to be kinetically stable below 500 °C and then decomposes completely to $BaCO_3$, CeO_2, and Y_2O_3 after exposure to pure CO_2 at 700–1000 °C [13,14]. The XRD spectra of $Ba(Zr_{0.4}Ce_{0.5})Y_{0.1}O_{2.95}$ and $Ba(Zr_{0.6}Ce_{0.3})Y_{0.1}O_{2.95}$ sintered pellets showed good chemical stability after being boiled in water or after being exposed to CO_2 at 900 °C [15].

In recent stability work, the calcined $Ba(Ce_{0.8-x}Zr_x)Y_{0.2}O_{3-\delta}$ powders synthesized by the sol–gel process exhibit a good chemical stability for $x > 0.5$ after exposure to CO_2 atmosphere at 900 °C for 3 h [16]. Similarly, XRD results of $Ba(Ce_{0.8-x}Zr_x)Y_{0.2}O_{3-\delta}$ powders prepared by the sol–gel process, show an obvious decomposition of $BaCO_3$ for $x \leq 0.4$ after treatment in a CO_2 atmosphere at 650 °C for 2 h [17]. These results suggest that proton-conducting solid solutions between cerate and zirconate may have both high proton conductivity

and good chemical stability [18]. $A^{II}B^{IV}O_3$-based proton conductors are doped in B-site by lower valence elements, typically Y^{3+} or trivalent rare-earth metal cations, creating oxygen vacancies. Subsequent exposure to humid atmospheres is presumed to lead to the incorporation of protons, resulting in proton conduction [19,20].

Many synthesis techniques have been used to fabricate $Ba(Zr,Ce)O_3$-based proton-conducting ceramic powders, including solid state reaction [21,22], co-precipitation [15], sol–gel [23], hydrothermal [24], and combustion [25,26]. The synthesis of ultrafine powders with controlled powder characteristics is important to make dense products at a lower sintering temperature [27]. Better conductivity in nano-crystalline materials compared to micro-structure samples has been reported in yttrium stabilized zirconia (YSZ) and Y_2O_3-doped ZrO_2 due to the higher grain boundary conductivity in nano-crystalline samples [28].

The glycine–nitrate process (GNP) using glycine as a fuel and nitrate as an oxidizer, attracts great interest because it can produce powders with greater compositional uniformity, lower residual carbon level, and nano-particle size [25]. Glycine (NH_2CH_2COOH), one of the cheapest amino acids, is used as a fuel and acts as a complexing agent for metal cations as it has a carboxylic acid group at one end and amino group at the other end. The zwitterionic character of a glycine molecule can effectively complex metal cations of varying ionic size, which increases their solubility and prevents selective precipitation as water is evaporated to maintain compositional homogeneity among the constituents. The site for the complexed cation depends on the size and charge of the cation, and the pH value. It has been recognized that alkali and alkaline-earth (Ba^{2+}) cations are effectively complexed by the carboxylic acid group, while transition metal cations (Zr^{4+},Y^{3+}) and rare-earth cations (Ce^{3+}) are effectively complexed by the amine group [25,29]. The glycine-to-nitrate (G/N) ratio needs to have sufficient glycine to retain complete complexation of the cations as the solution is being evaporated.

A key question is the particle size obtained by the glycine–nitrate process (GNP) compared to that obtained by solid state reaction (SSR). A comparison from our group [8] found that by both XRD and transmission electron microscopy (TEM), the GNP powder had 21 nm size, whereas by TEM the SSR powder had about 100 nm size, too large to determine by XRD using Scherrer's equation. Planetary ball milling can reduce the SSR particle size, but this process requires added time and expense.

Though proton-conducting ceramics are promising candidates for SOFC applications, one of the major issues for these materials is to find appropriate components with single-phase structure and low densification temperature. In addition, although the combustion synthesis route has been used for fabrication of BCZY powders, the optimizing condition for the G/N ratio for various Zr/Ce contents had not previously been investigated systematically. In this work, X-ray diffraction (XRD) and micro-Raman spectroscopy were employed to investigate crystallization, structural phase, and particle size of BZCY ($x = 0.0$–0.8) ceramic powders synthesized by the GNP as functions of G/N and Zr/Ce molar ratios. Field emission scanning electron microscope (FESEM) and TEM were used to obtain morphologies of as-synthesized BZCY712 powders fabricated with various G/N ratios. In addition, in-situ temperature-dependent dilatometry was used to study the effect of particle size on densification (or sintering) temperature.

2. Experimental procedure

The starting materials were $Ba(NO_3)_2$ (Alfa Aesar, 99.95%), $ZrO(NO_3)_2 \cdot xH_2O$ (Alfa Aesar, 99.9%), $Ce(NO_3)_3 \cdot 6H_2O$ (Alfa Aesar, 99.9%), and $Y(NO_3)_3 \cdot 6H_2O$ (Alfa Aesar, 99.9%) metal nitrate powders. Each was dissolved in deionized water to make the metal nitrate solution. The appropriate molar ratios of the nitrates and glycine were mixed to obtain a solution. The solution then was heated and stirred at 150–200 °C to evaporate excess water. The resulting viscous liquid auto-ignited and produced the desired powders. Since this work mainly investigates the particle size effect of synthesis processes, the grinding (or milling) process was not used before and after calcinations.

The stoichiometric GNP combustion reaction occurs according to the following reaction equation, in which the amounts of the gaseous products of CO_2, N_2, and H_2O are not specified:

$$Ba(NO_3)_{2(aq)} + (0.8-x)ZrO(NO_3)_{2(aq)} + xCe(NO_3)_{3(aq)} + 0.2Y(NO_3)_{3(aq)} + \alpha NH_2CH_2COOH_{(aq)} \rightarrow Ba(Zr_{0.8-x}Ce_xY_{0.2})O_{2.9(c)} + CO_{2(g)} + N_{2(g)} + H_2O_{(g)} \quad (1)$$

According to the principles of propellant chemistry [30], the ratio of the net oxidizing valence of the metal nitrate to the net reducing

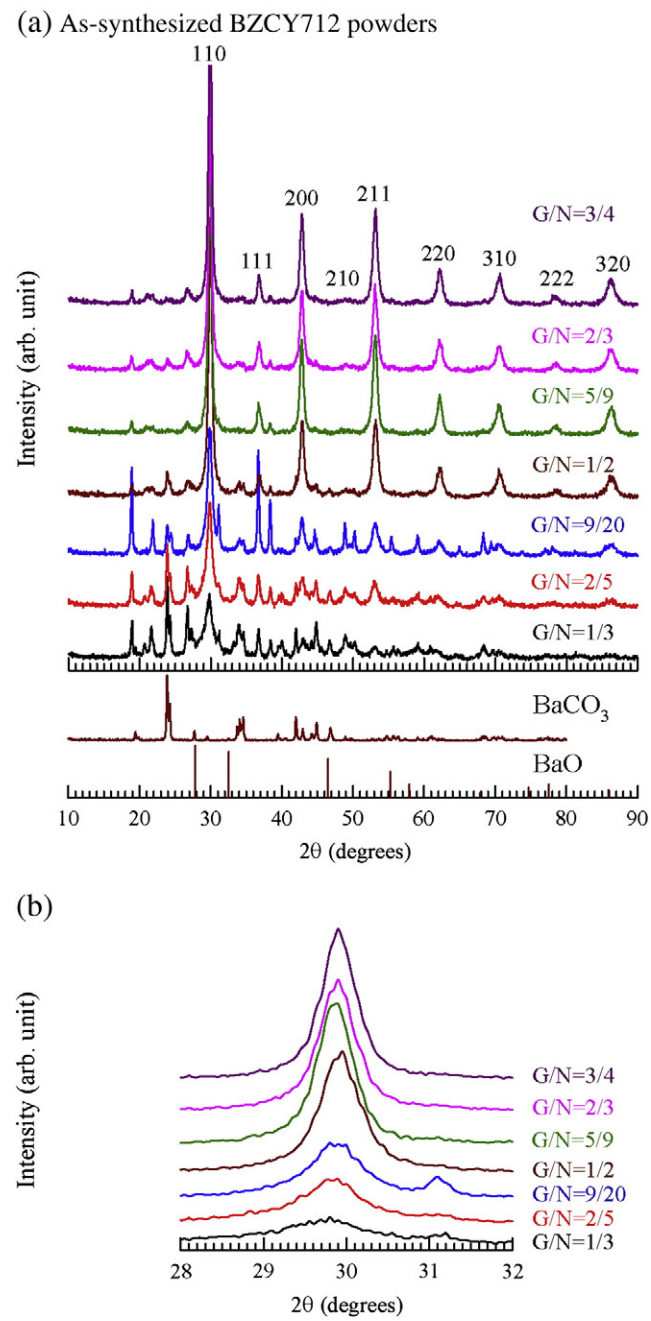

Fig. 1. (a) XRD spectra of as-synthesized BZCY712 powders synthesized with various G/N ratios, $BaCO_3$ powder (99.9%), and BaO powder. (b) Enlarged (110) XRD peaks.

valence of the fuel should be unity. The extrapolation of this concept to the combustion synthesis of ceramic oxides means that metals like barium, cerium, and yttrium (or any other metals) should be considered as reducing elements with the valences they have in the corresponding oxides, i.e. +2, +3, and +3, respectively. Therefore, the total oxidizing valence of nitrates is $-21-5x$, whereas the total reducing valence of NH_2CH_2COOH is +9, so the stoichiometric redox reaction can be expressed as:

$$\begin{aligned}&Ba(NO_3)_2+(0.8-x)ZrO(NO_3)_2+xCe(NO_3)_3+0.2Y(NO_3)_3\\&+[(21+5x)/9]NH_2CH_2COOH+(x/4)O_2\rightarrow Ba(Zr_{0.8-x}Ce_xY_{0.2})O_{2.9}\\&+[(42+10x)/9]CO_2+[(49/15)+(7x/9)]N_2+[(105+25x)/18]H_2O\end{aligned} \quad (2)$$

By comparing Eqs. (1) and (2), we find that $\alpha=(21+5x)/9$ is the "stoichiometric glycine-to-barium nitrate molar ratio". The stoichiometric glycine-to-nitrate molar ratio (G/N) is $\alpha/(4.2+x)=5/9$, because for $x=0$ there are 4.2 times as many nitrate ions as metal ions in the nitrates [31]. For example, the stoichiometric glycine-to-barium nitrate and G/N molar ratios of $Ba(Zr_{0.7}Ce_{0.1}Y_{0.2})O_{2.9}$ (BZCY712) are $\alpha=21.5/9$ and $G/N=5/9$, respectively. Note that some papers used glycine-to-metal nitrate molar ratio as G/N molar ratio [32,33].

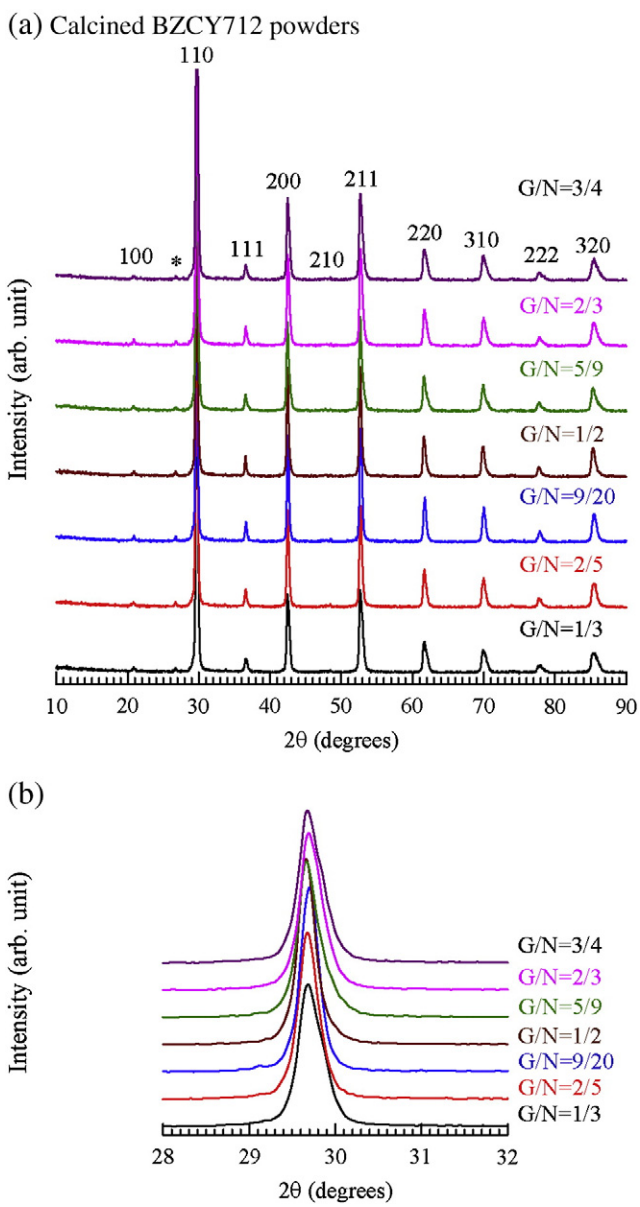

Fig. 2. (a) XRD spectra of calcined BZCY712 powders synthesized with various G/N ratios. (b) Enlarged (110) XRD peaks. "*" indicates a second phase.

To investigate structure (or phase) and particle size, a Rigaku Model MultiFlex X-ray diffractometer with Cu $K\alpha_1$ ($\lambda=0.15406$ nm) and Cu $K\alpha_2$ ($\lambda=0.15444$ nm) radiations was used. The intensity ratio between $K\alpha_1$ and $K\alpha_2$ is about 2:1 [34]. The 2θ-reflection angle and d spacing obey the Bragg's Law, $2d\sin\theta=n\lambda$. All calcined powders were performed at 1400 °C for 5 h in the laboratory air. Particle sizes of as-synthesized and calcined BZCY powders were estimated by using full width at half maxima (FWHM) of the major (110) XRD peak with the Scherrer's formula assuming spherical particles, i.e.,

$$D=\frac{0.9\lambda}{\beta\cos\theta} \quad (3)$$

where D is the particle size, λ is the x-ray radiation wavelength, θ is the angle of XRD peak, and β (in radians) is the FWHM of the XRD peak. θ and β were determined by using the PeakFit software with the sum of Gaussian and Lorentzian profiles to fit the XRD peak.

For in-situ temperature-dependent linear shrinkage measurement, a LINSEIS Model L75 dilatometer was used to study the effect of the particle size on densification (or sintering) temperature. Green pellets of 1/2 in. in diameter and 1–2 mm in thickness were prepared by pressing the ceramic powders uniaxially at 350 MPa for about 2 min. For micro-Raman spectroscopy, a double grating Jobin Yvon Model U-1000 double monochromator and a nitrogen-cooled CCD as a detector were employed. A Coherent Model Innova 90 argon laser of wavelength $\lambda=514.5$ nm was used as an excitation source.

Morphologies of as-synthesized BZCY712 pressed powders fabricated with various G/N ratios (1/3, 2/5, 9/20, 1/2, 5/9, 2/3, and 3/4) were taken by Hitachi Model S-80 FESEM. The Hitachi Model H-7100 Model TEM was used to investigate particle size of as-synthesized BZCY 712 powder fabricated with G/N ratio of 1/2.

3. Results and discussion

Figs. 1 and 2 show XRD spectra of as-synthesized and calcined BZCY712 powders fabricated with various G/N ratios from 1/3 to 3/4. For as-synthesized BZCY712 powders (Fig. 1(a)), the G/N ratios near

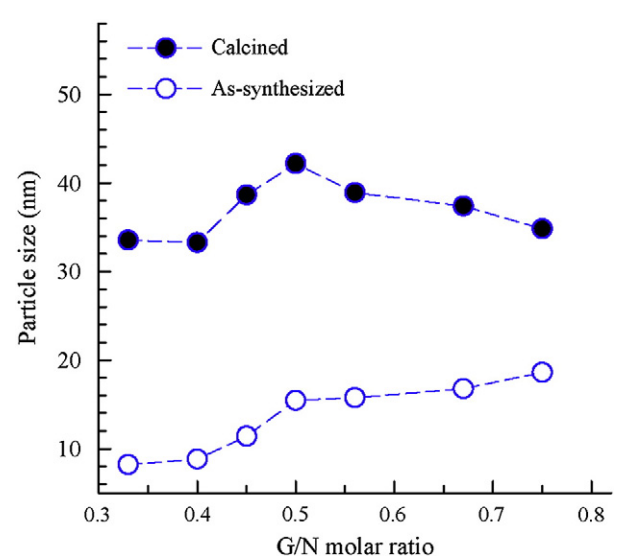

Fig. 3. Particle sizes of as-synthesized and calcined BZCY712 powders as a function of G/N ratio.

and above stoichiometric ratio of 5/9 yield better crystallization and a nearly single-phase structure mixed with minor $BaCO_3$, possible BaO, and other second phases, possibly due to incomplete reaction. After calcination at 1400 °C for 5 h in air, BZCY712 powders of various G/N ratios exhibit similar single-phase XRD spectra with a weak second phase as indicated by "*" in Fig. 2(a). $BaCO_3$ and BaO were not observed after calcination at 1400 °C. The main 2θ peaks including (100), (110), (111), (200), (210), (211), (220), (310), (222), and (320) suggest a simple cubic structure according to a structure-factor calculation [34]. The cubic lattice parameters estimated from the (110) peaks are $a \cong 4.209$ Å and $a \cong 4.279$ Å for as-synthesized and calcined BZCY712 powders, respectively.

Particle sizes of as-synthesized and calcined BZCY712 powders were estimated by using Eq. (3) and full width at half maxima

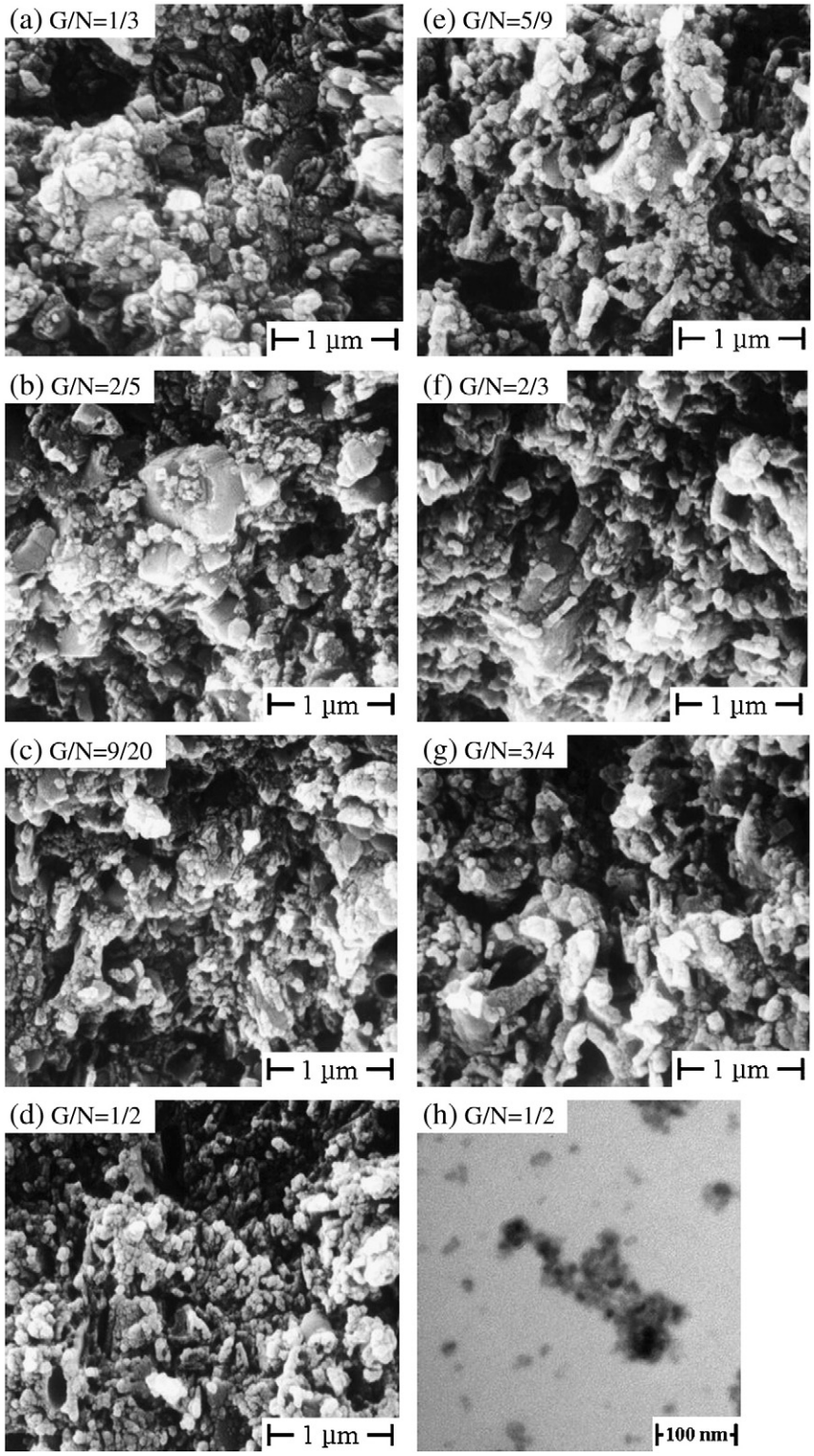

Fig. 4. FESEM morphologies of as-synthesized BZCY712 pressed powders fabricated with G/N ratios of (a) 1/3, (b) 2/5, (c) 9/20, (d) 1/2, (e) 5/9, (f) 2/3, and (g) 3/4. (h) TEM morphology of as-synthesized BZCY powder fabricated with G/N ratio of 1/2.

(FWHM) of the (110) XRD peaks as enlarged in Figs. 1(b) and 2(b). Particle size of as-synthesized BZCY712 increases as the G/N ratio increases. Note that the theoretical adiabatic flame temperature increases as stoichiometric glycine-to-barium nitrate molar ratio α (or G/N molar ratio) increases. As shown in Fig. 3, particle sizes of as-synthesized and calcined BZCY712 powders vary in the ranges of ~8–20 nm and ~26–42 nm, respectively. Calcined BZCY712 powders exhibit a maximum of particle size for G/N = 1/2. Fig. 4 shows FESEM and TEM morphologies of as-synthesized BZCY712 powders fabricated by the GNP with various G/N ratios. The average particle size of as-synthesized BZCY712 powders with G/N = 1/2 was estimated from TEM result and is about 15 nm, which is consistent with the particle size in Fig. 3 estimated from the FWHM of the (110) XRD spectrum.

Fig. 5 shows temperature-dependent linear shrinkage measurement upon heating for the pellets prepared from the calcined and as-synthesized BZCY712 powders fabricated with G/N = 1/2. The pellet pressed from as-synthesized powders with particle size of ~15 nm begins densification near 1000 °C, which is about 200 °C lower than the densification temperature of the pellet from the calcined powders (particle size ~45 nm). This indicates that finer nano-size powders are important for fabricating dense ceramics at a lower sintering temperature.

In related work by our group, it was found that use of LiF sintering aid dramatically decreases sintering temperature for ceramics made by the glycine–nitrate process [35]. The LiF sintering aid was not tried with ceramics made by solid state reaction. However, because the glycine–nitrate process gives smaller-particle size and correspondingly smaller gaps between grains, and the role of the LiF is to coat and lubricate grain surfaces, it seems likely that the advantage of using LiF would be greater for ceramics made by the glycine–nitrate process.

To investigate the effect of Zr/Ce molar ratio on structure and particle size, G/N = 1/2 was used to synthesize BZCY (x = 0.0–0.8) powders. As shown in Fig. 6(a), the Zr/Ce molar ratios ≥ 5/3 result in close to a single-phase structure mixed with $BaCO_3$ and second phases. After calcination at 1400 °C for 5 h in air, single-phase BZCY (x = 0.0–0.8) powders were obtained for all compounds as shown in Fig. 6(b). In addition, calcined BZCY powders for Zr/Ce ≤ 2/6 exhibit obvious two-peak splitting (Fig. 6(b)) and disappearance of the (100) peak, indicating a structural transformation from the simple cubic phase to possibly rhombohedral phase mixed with a monoclinic phase [36,37]. As indicated by the dashed line in Fig. 6(b), the (110) peak shifts toward higher 2θ reflection angle as Zr/Ce ratio

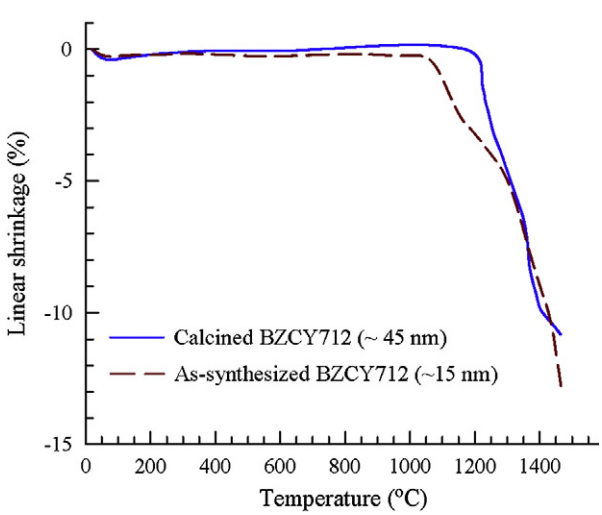

Fig. 5. Linear shrinkage vs. temperature of calcined and as-synthesized BZCY712 with the average particle sizes of ~45 nm and ~15 nm, respectively. The calcined sample thickness was 0.9 mm and the as-synthesized sample thickness was 1.26 mm.

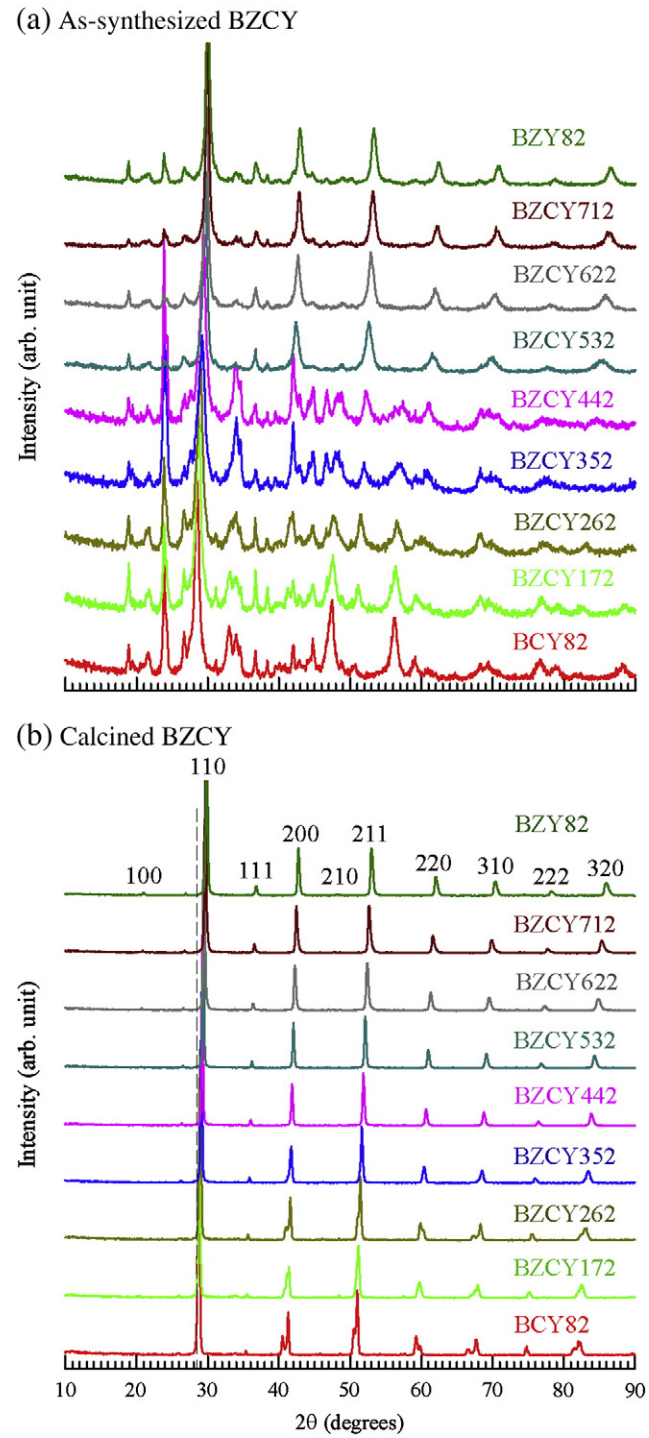

Fig. 6. XRD spectra of (a) as-synthesized and (b) calcined BZCY powders synthesized with G/N = 1/2. The dashed line indicates the shift of (110) peak.

increases. The lattice d spacings of BZY82 (2.991 Å), BZCY712 (3.011 Å), BZCY622 (3.026 Å), BZCY532 (3.036 Å), BZCY442 (3.051 Å), BZCY352 (3.066 Å), BZCY262 (3.087 Å), BZCY172 (3.092 Å), and BCY82 (3.113 Å) increase with increasing Ce content because the radius of Ce^{4+} (R^{IV} = 0.87 Å) is larger than for Zr^{4+} (R^{IV} = 0.72 Å) [38]. By using Eq. (3) to fit the FWHM of (110) XRD peak, particle sizes of the as-synthesized and calcined BZCY (x = 0.0–0.8) powders were estimated as shown in Fig. 7. Particle sizes of the as-synthesized and calcined BZCY (x = 0.0–0.8) powders vary in the ranges of ~5–15 nm and ~34–42 nm, respectively. Both as-synthesized and calcined BZCY (x = 0.0–0.8) powders fabricated

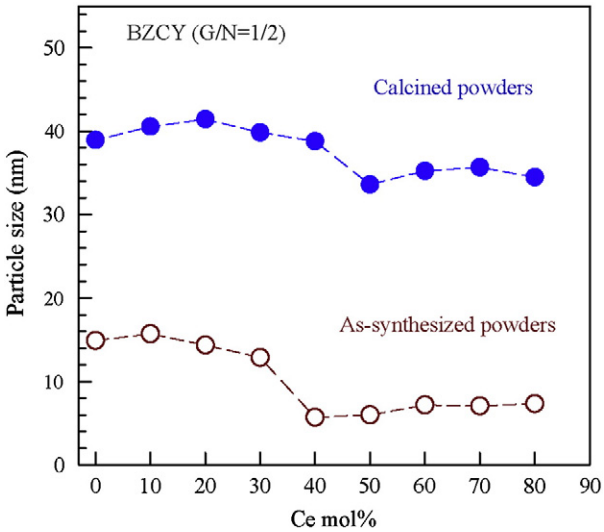

Fig. 7. Particle sizes of as-synthesized and calcined BZCY powders as a function of Ce mol%.

with $G/N = 1/2$ exhibit a minimum in particle size for ~50 mol% of cerium.

Fig. 8(a) and (b) show micro-Raman spectra of as-synthesized and calcined BZCY ($x = 0.0$–0.8) powders, respectively. As-synthesized BZCY powders exhibit relatively strong Raman modes of $BaCO_3$ near 690 and 1060 cm^{-1} as indicated by "+", which correspond respectively to the doubly degenerate bending mode (E″) and symmetric stretching vibration (A'_1) of the CO_3^{2-} ion [39]. The Raman spectrum of $BaCO_3$ can be found in Ref. 29. The splitting of the 1060 cm^{-1} mode implies that the CO_3^{2-} ion has different chemical environments due to incomplete reaction. The vibration mode at 730 cm^{-1} (as indicated by "#") possibly associates with a second phase. The broad Raman peak in the region of 460–480 cm^{-1} likely corresponds to the $(Ce,Zr)O_2$-like structure, because the major Raman lines of CeO_2 and ZrO_2 powders appear respectively at 461 and 474 cm^{-1} [40]. The 461 cm^{-1} vibration of CeO_2 results from the F_{2g} mode of the fluorite structure [41]. The 474 cm^{-1} vibration of ZrO_2 corresponds to the A_g mode of the O–O vibration [42]. As Zr content increases (Fig. 8(a)), the 460 cm^{-1} vibration (for BCY82) shifts toward higher frequency and its relative intensity decreases as well.

Calcined BZCY ($x = 0.0$–0.8) powders exhibit similar Raman spectra for vibrations of ≥ 400 cm^{-1} as shown in Fig. 8(b). The vibration frequency shifts toward higher value as Zr/Ce ratio increases due to the reduction of effective atomic mass. It is important to note that Raman modes for $Zr/Ce \leq 2/6$ exhibit obviously different profiles and relative intensities in the region of 300–400 cm^{-1}, indicating a structural transformation as evidenced in XRD of Fig. 6(b). Raman vibrations of 690 and 1060 cm^{-1} for $BaCO_3$ were not observed in calcined BZCY ($x = 0.0$–0.8) powders, implying that calcination at 1400 °C completes the chemical reaction. This is consistent with the XRD spectra of calcined BZCY powders as seen in Fig. 6(b), in which $BaCO_3$ structure was not found. The major Raman modes of calcined BZCY powders occur in the regions of 340–380 cm^{-1} and 640–720 cm^{-1}. Note that the main Raman mode of Y_2O_3 appears near 375 cm^{-1}. Thus, the vibrations of 340–380 cm^{-1} likely correspond to Raman modes of Y_2O_3-like structure. The Raman modes of 440–500 cm^{-1} as a shoulder on the left-hand side of the major vibrations (340–380 cm^{-1}), likely correspond to vibrations of $(Ce,Zr)O_2$-like structure.

4. Conclusions

Proton-conducting BZCY ($x = 0.0$–0.8) ceramic powders are synthesized by the GNP as functions of G/N and Zr/Ce molar ratios and

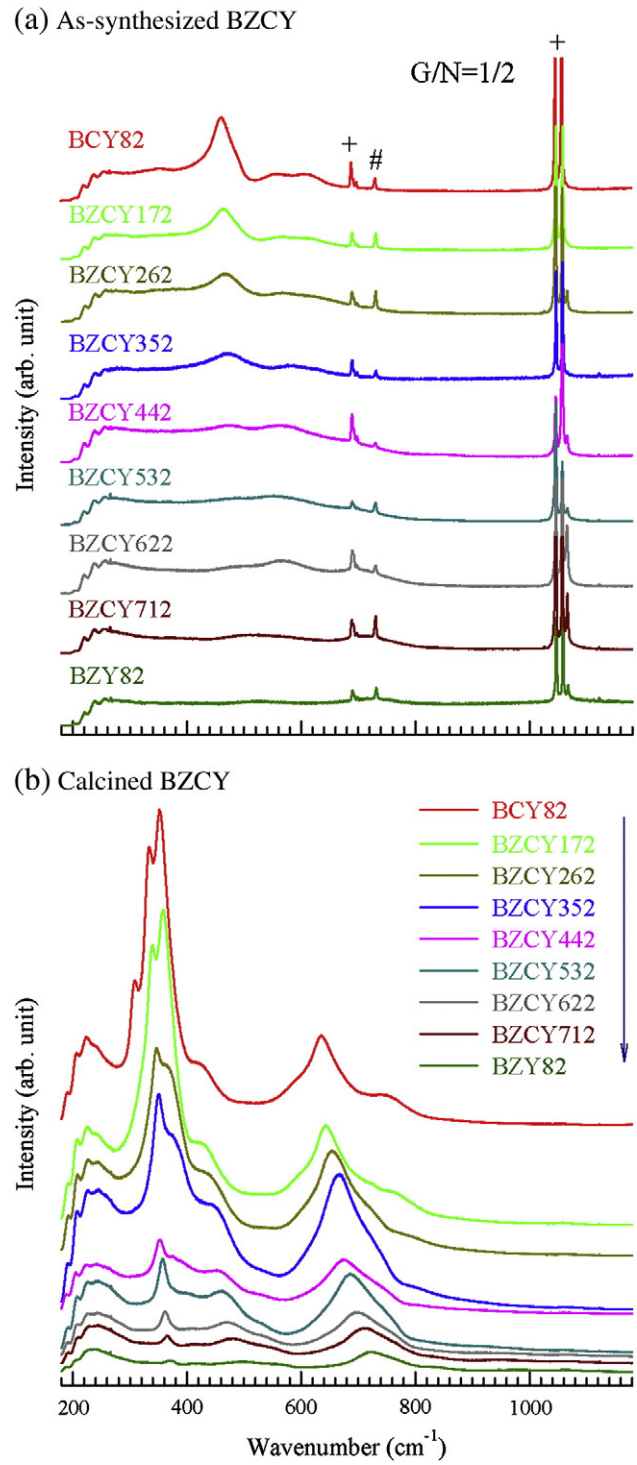

Fig. 8. Raman spectra of (a) as-synthesized and (b) calcined BZCY powders synthesized with $G/N = 1/2$. "+" and "#" correspond to vibration frequencies of $BaCO_3$ and a possible second phase, respectively.

their structural properties have been characterized by using XRD and micro-Raman spectroscopy. For as-synthesized BZCY712 powders, the G/N ratios near and slightly above stoichiometric ratio (5/9) yield better crystallization and a nearly single-phase structure mixed with minor $BaCO_3$ and second phases. Particle size of the as-synthesized BZCY712 powders increases as G/N ratio increases, i.e. the theoretical adiabatic flame temperature increases. Calcined BZCY712 powders fabricated with various G/N ratios (1/3–3/4) exhibit an expected simple cubic perovskite structure and larger particle sizes compared to

as-synthesized powders. Smaller-particle BZCY712 powders can reach densification at a lower sintering temperature. As-synthesized BZCY (Zr/Ce ≥ 5/3) powders fabricated with G/N = 1/2 result in a nearly single-phase structure. Calcined BZCY ($x = 0.0$–0.8) powders exhibit a single-phase structure for all compounds. X-ray diffraction and Raman scattering spectroscopy confirm that calcined BZCY powders for Zr/Ce ≤ 2/6 exhibit a structural transformation from cubic to possibly rhombohedral (mixed with monoclinic). Particle sizes of as-synthesized and calcined BZCY ($x = 0.0$–0.8) powders are sensitive to Zr/Ce ratio, and vary in the ranges of 5–15 nm and ~34–42 nm, respectively.

Acknowledgements

The authors would like to thank Dr. J. Liang (Fu Jen Catholic University) for the Raman scattering apparatus. This work was supported by DOE under subcontract DEAC06-76RL01830 from Battelle Memorial Institute and PNNL, and National Science Council of Taiwan Grant no. 96-2112-M-030-001.

References

[1] H. Iwahara, T. Esaka, H. Uchida, N. Maeda, Solid State Ionics 3/4 (1981) 359.
[2] H. Iwahara, H. Uchida, K. Kondo, K. Ogaki, J. Electrochem. Soc. 135 (1988) 529.
[3] H. Iwahara, Solid State Ionics 77 (1995) 289.
[4] N. Taniguchi, T. Kuroha, C. Nishimura, K. Iijima, Solid State Ionics 176 (2005) 2979.
[5] L. Yang, C. Zuo, S. Wang, Z. Cheng, M. Liu, Adv. Mater. 20 (2008) 3280.
[6] G. Meng, G. Ma, Q. Ma, R. Peng, X. Liu, Solid State Ionics 178 (2007) 697.
[7] L. Yang, S. Wang, K. Blinn, M. Liu, Z. Liu, Z. Cheng, Science 326 (2009) 126.
[8] C.-L. Tsai, Ph.D. Thesis, Montana State University (May 2010).
[9] N. Bonanos, K.S. Knight, B. Ellis, Solid State Ionics 79 (1995) 161.
[10] C.W. Tanner, A.V. Virkar, J. Electrochem. Soc. 143 (1996) 1386.
[11] J. Li, J.-L. Luo, K.T. Chuang, A.R. Sanger, Electrochim. Acta 53 (2008) 3701.
[12] K.D. Kreuer, Solid State Ionics 97 (1997) 1.
[13] N. Zakowsky, S. Williamson, J.T.S. Irvine, Solid State Ionics 176 (2005) 3019.
[14] B.R. Sneha, V. Thangadurai, J. Solid State, Chemistry 180 (2007) 2661.
[15] Z. Zhong, Solid State Ionics 178 (2007) 213.
[16] E. Fabbri, A. D'Epifanio, E.D. Bartolomeo, S. Licoccia, E. Traversa, Solid State Ionics 179 (2008) 558.
[17] Y. Guo, Y. Lin, R. Ran, Z. Shao, J. Power, Sources 193 (2009) 400.
[18] C. Zuo, S. Zha, M. Liu, M. Hatano, M. Uchiyama, Adv. Mater. 18 (2006) 3318.
[19] T. Norby, M. Widerøe, R. Glöckner, Y. Larring, Dalton Trans. (2004) 3012.
[20] K.D. Kreuer, Annu. Rev. Mater. Res. 33 (2003) 333.
[21] K. Katahira, Y. Kohchi, T. Shimura, H. Iwahara, Solid State Ionics 138 (2000) 91.
[22] K.H. Ryu, S.M. Haile, Solid State Ionics 125 (1999) 355.
[23] R.B. Cervera, Y. Oyama, S. Yamaguchi, Solid State Ionics 178 (2007) 569.
[24] W. Zheng, C. Liu, Y. Yue, W. Peng, Mater. Lett. 30 (1997) 93.
[25] L.A. Chick, L.R. Pederson, G.D. Maupin, J.L. Bates, L.E. Thomas, G.J. Exarhos, Mater. Lett. 10 (1990) 6.
[26] P. Babilo, T. Uda, S.M. Haile, J. Mater. Res. 22 (2007) 1322.
[27] Y. Zhou, M.N. Rahaman, Acta Mater. 45 (1997) 3635.
[28] N.H. Perry, S. Kim, T.O. Mason, J. Mater. Sci. 43 (2008) 4684.
[29] S.L. Gao, X.W. Yang, D.H. Ren, Q.Z. Shi, Thermochim. Acta 287 (1996) 177.
[30] S.R. Jain, K.C. Adiga, V.R. Pai Verneker, Combust. Flame 40 (1981) 71.
[31] R.D. Purohit, B.P. Sharma, K.T. Pillai, A.K. Tyagi, Mater. Res. Bull. 36 (2001) 2711.
[32] W. Chen, F. Li, J. Yu, Mater. Lett. 60 (2006) 57.
[33] M. Jacquin, Y. Jing, A. Essoumhi, G. Taillades, D.J. Jones, J. Rozière, J. New Mater, Electrochem. Syst. 10 (2007) 243.
[34] B.D. Cullity, Elements of X-ray Diffraction, 2nd editionAddison Wesley Publishing, 1978.
[35] C.-L. Tsai, M. Kopczyk, R.J. Smith, V.H. Schmidt, Solid State Ionics 181 (2010) 1083.
[36] K. Takeuchia, C.-K. Loong, J.W. Richardson Jr., J. Guanb, S.E. Dorris, U. Balachandran, Solid State Ionics 138 (2000) 63.
[37] C.-K. Loong, M. Ozawa, K. Takeuchi, K. Ui, N. Koura, J. Alloys Compd. 408–412 (2006) 1065.
[38] R.D. Shannon, Acta Crystallographia A32 (1976) 751.
[39] R.L. Frost, J.M. Bouzaid, J. Raman, Spectroscopy 38 (2007) 873.
[40] C.-S. Tu, R.R. Chien, V.H. Schmidt, S.-C. Lee, C.-C. Huang, C.-L. Tsai, J. Appl. Phys. 105 (2009) 103504 (1-7).
[41] R.Q. Long, Y.P. Huang, H.L. Wan, J. Raman, Spectroscopy 28 (1997) 29.
[42] B.-K. Kim, H.-O. Hamaguchi, Phys. Stat. Sol. (b) 203 (1997) 557.